Supplemental material for: Fast microscale acoustic streaming driven by a temperature-gradient-induced non-dissipative acoustic body force

Wei Qiu,[1,*] Jonas Helboe Joergensen,[2,†] Enrico Corato,[1] Henrik Bruus,[2,‡] and Per Augustsson[1,§]

[1] *Department of Biomedical Engineering, Lund University, Ole Römers väg 3, 22363 Lund, Sweden*

[2] *Department of Physics, Technical University of Denmark, DTU Physics Building 309, DK-2800 Kongens Lyngby, Denmark*

(Dated: 24 June 2021)

This supplemental material provides details about the temperature measurements, the comparison between measured and simulated temperature fields, the numerical model, as well as the measured and simulated Rayleigh-Bénard convection.

S1. TEMPERATURE MEASUREMENTS

The temperature gradients inside the microchannel were measured in x-y plane using an aqueous 1-mM solution of the temperature-sensitive fluorescent dye rhodamine B that has a peak wavelength at 554 nm, which is outside the absorption range of Orange G. Thus fluorescence imaging of rhodamine B molecules did not affect the temperature gradients produced by the light absorption of Orange G molecules. The optical properties of each substance used in the solution are summarized in Table S1.

The temperature dependence of dye fluorescence intensity for each pixel was obtained using the setup shown in Fig. S1. Two 1-mm-thick aluminum plates with two Peltier elements make contact with the two edges of the silicon layer of the microchip. Constant temperature inside the channel was obtained by applying the same temperature to both Peltier elements from 22 ℃ to 42 ℃ with an interval of 4 ℃ using a PID control loop from the resistance thermometer Pt1000. Through a 2D simulation of heat transfer including air cooling in an extreme case with the temperature of the Peltier elements and the air set to 42 ℃ and 25 ℃, respectively, we confirmed that the maximum temperature difference between the Peltier elements and the microchannel is less than 0.09 ℃, and the maximum temperature difference in the microchannel is less than 0.03 ℃, see Fig. S2. The dye fluorescence intensity for each temperature was recorded with the camera focal plane placed at the channel mid-height $z = 0$ µm. The intensity at each pixel was calculated by averaging in total 27 frames recorded for each temperature, with an exposure time of 11 ms and a frame rate of 20 fps. Noise was reduced by a 3×3 mean filter. The intensity at all pixels far from the sidewalls decreases linearly as temperature increases (Fig. S3), which agrees with the literature [1], and pixel-wise calibration curves were used to calculate the temperature value at each pixel to eliminate the effect of aberration-induced spatial variations in

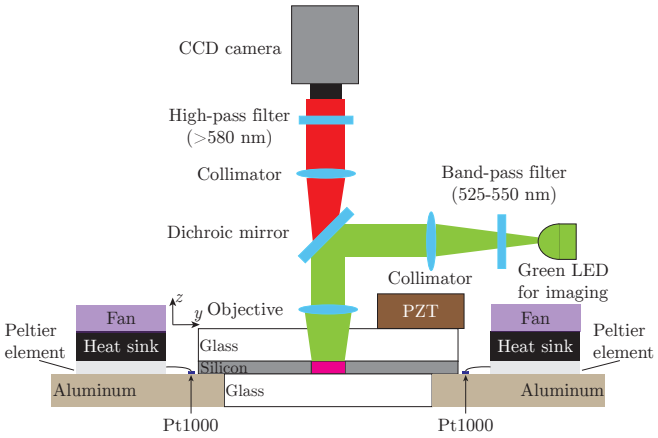

FIG. S1. Sketch of the calibration setup for temperature measurements. Two 1-mm-thick aluminum plates with two Peltier elements sitting on top make contact with the two edges of the silicon layer of the microchip to create uniform temperature field inside the microchannel. The temperature control of the Peltier elements are assisted by heat sinks and fans with a PID control loop from the resistance thermometer Pt1000 (blue). Temperature-sensitive fluorescent dye (rhodamine B, pink) is mixed with the medium, and green light is used to excite its fluorescence which is acquired by the CCD camera. The transducer ($25 \times 6 \times 2$ mm^3) is made of PZT Pz26 (Meggitt Ferroperm Piezoceramics, Kvistgaard, Denmark).

TABLE S1. The optical properties of the Orange G (Sigma-Aldrich, St. Louis, MO) and rhodamine B (Acros Organics, Fair Lawn, NJ) solutions as well as the 1.1 µm-diameter tracer particles (Thermo Fisher Scientific, Waltham, MA) used in experiments.

Substance	Absorption peak	Emission peak
Orange G	478 nm	–
Rhodamine B	554 nm	575 nm
Tracer particles	542 nm	612 nm

* wei.qiu@bme.lth.se
† jonashj@fysik.dtu.dk
‡ bruus@fysik.dtu.dk
§ per.augustsson@bme.lth.se

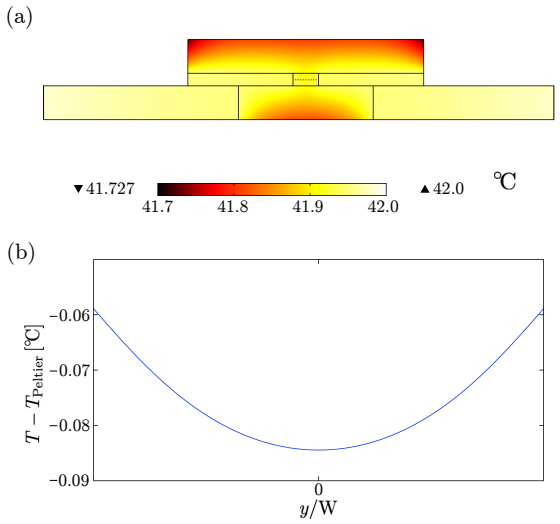

FIG. S2. (a) Color plot from 41.7 ℃ (black) to 42 ℃ (white) of the simulated heat transfer including air cooling with the temperature of the Peltier elements and the air set to $T_{\mathrm{Peliter}} = 42$ ℃ and $T_{\mathrm{air}} = 25$ ℃, respectively. (b) The difference between the temperature in the microchannel T and T_{Peliter} along the channel width at channel mid-height, indicated by the brown dashed line in panel (a).

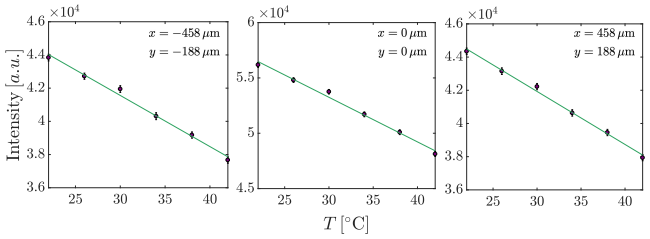

FIG. S3. The measured dye fluorescence intensity as a function of temperature at three arbitrary positions inside the microchannel. The intensity at all pixels far from the sidewalls shows linear decrease as temperature increases.

the optical signal. The absorption of rhodamine B in water varies less than 2% within the temperature range in our measurements [2], thus the fluorescence intensity is not affected by the different absorption levels at different temperatures.

The liquid was heated by shinning the blue LED from below, the ultrasound field was activated, and the corresponding dye fluorescence intensity was recorded and converted to temperature using pixel-wise calibration curves, see Fig. S4. It is worth noting that this method is not applicable to measure the temperature close to the walls, in our case within 50 µm, mainly because of the light scattering when walls are present. Hence, the obtained temperature dependence of dye fluorescence intensity close to the walls is error prone. This error can only be minimized by using specific wall materials and optical configurations [3], which is hard to perform in our acoustofluidic devices. We therefore excluded regions within a distance of 50 µm from the silicon sidewalls, indicated by gray in Fig. S4. The mapped temperature field was then fitted by a 2D Gaussian function to determine the temperature difference ΔT_0 across the channel and the corresponding temperature gradient $G = 2\Delta T_0/W$. The resolution of dye fluorescence intensity variation was not sufficiently high for ΔT_0 below 1 K, and the two lowest temperature gradients were therefore extrapolated based on the linear dependence of temperature on the LED power. We have not attempted to resolve the temperature variation along the z-direction due to the intricate influence of the fluorescence intensity on the focal plane from the adjacent planes.

S2. COMPARISON BETWEEN MEASURED AND SIMULATED TEMPERATURE FIELDS

The images acquired by the compound microscope are convoluted in all three directions, and are therefore difficult to directly compare with the simulated temperature field which provides a super-resolution temperature value at each position. Thus, we first determined the point spread functions (PSFs) in all three directions in our imaging system using Gaussian approximations [4]

$$g(x,y,z) = A\exp(-\frac{x^2+y^2}{2\sigma_{xy}^2} - \frac{z^2}{2\sigma_z^2}), \tag{S1a}$$

$$\sigma_{xy} = \frac{\sqrt{2}}{k_{\mathrm{em}}\mathrm{NA}}, \tag{S1b}$$

$$\sigma_z = \frac{2\sqrt{6}n}{k_{\mathrm{em}}\mathrm{NA}^2}, \tag{S1c}$$

where $k_{\mathrm{em}} = 2\pi/\lambda_{\mathrm{em}}$, n, and NA are the emission wavenumber, the refractive index of the liquid, and the numerical aperture of the objective lens, respectively. The calculated PSFs in the x-y plane and the z direction for the imaging system are plotted in Fig. S5. The PSFs in the x-y plane drop to zero within 2×2 µm^2, which is close to the smooth filter size of 3×3 pixels that was used to obtain the pixel intensity (each pixel has a size of 0.641×0.641 µm^2), and thus the effect of convolution in the x-y plane can be neglected. Along the z axis the intensity value was convoluted in a range of 50 µm. Considering that the PSF in z direction $g(z)$ is symmetric, the convoluted intensity in experiments I_z^{con} can be written in its discrete form as

$$I_z^{\mathrm{con}} = I_z^{\mathrm{sup}} * g(z) = \sum_{i=1}^{N} I_{z_i}^{\mathrm{sup}} g(z_i), \tag{S2}$$

where I_z^{sup} is the super-resolution intensity in the z direction and z_i with $i = 1, \ldots, N$ are the discrete grid points in the same direction corresponding to the mesh elements in the simulation. When the temperature is uniform along the z direction, which is the case for calibration, the linear dependence of dye fluorescence intensity

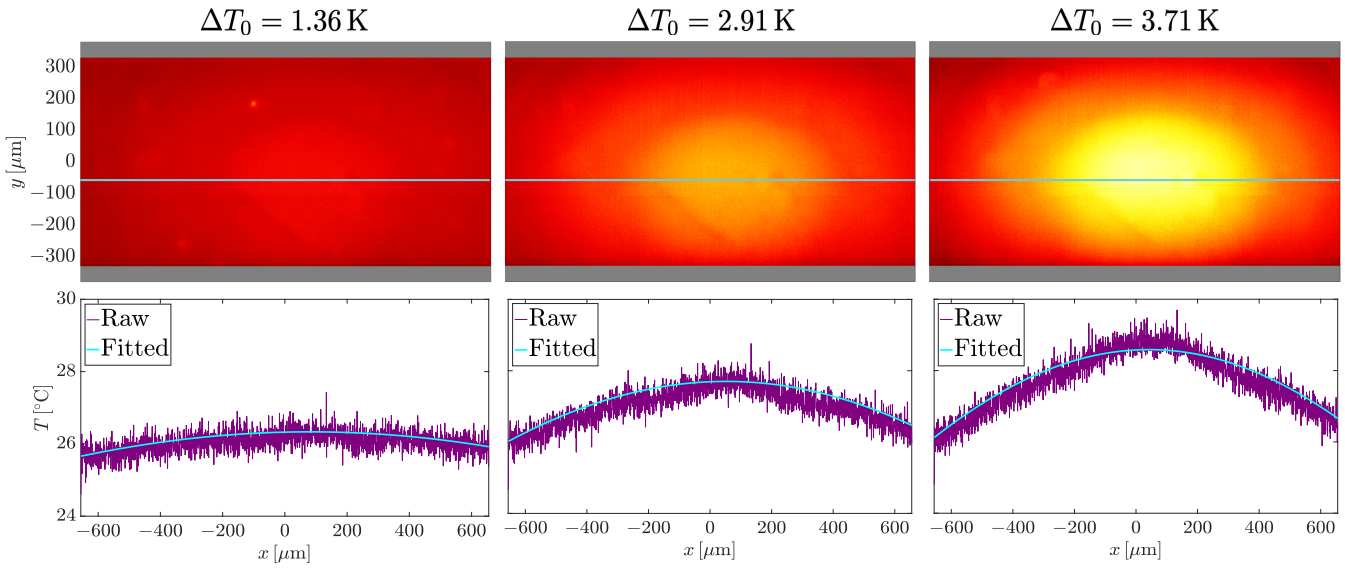

FIG. S4. The upper row: Color plots of the mapped temperature fields in the x-y plane around $z = 0$ µm from 23.7 (black) to 30 ℃ (white) at $\Delta T_0 = 1.36$, 2.91, and 3.71 K. Regions where the fluorescence intensity is affected by the channel sidewalls are excluded (gray). The lower row: Line plots of the raw (purple) and fitted (cyan, 2D Gaussian fit) temperature along the respective cyan lines in the above color plots. ΔT_0 is determined by the difference between the maximum and minimum values in the fitted temperature profile.

on temperature can be expressed as

$$I_z^{\mathrm{sup}} = a^{\mathrm{sup}} T + b^{\mathrm{sup}}, \tag{S3a}$$
$$I_z^{\mathrm{con}} = a^{\mathrm{con}} T + b^{\mathrm{con}}, \tag{S3b}$$

where the superscripts "sup" and "con" denote super-resolution and convoluted cases. Combining Eqs. (S2) and (S3), we obtain

$$a^{\mathrm{sup}} \sum_{i=1}^{N} g(z_i) T + b^{\mathrm{sup}} \sum_{i=1}^{N} g(z_i) = a^{\mathrm{con}} T + b^{\mathrm{con}}. \tag{S4}$$

Therefore, the relationship between super-resolution and convoluted coefficients are found to be

$$a^{\mathrm{con}} = a^{\mathrm{sup}} \sum_{i=1}^{N} g(z_i), \tag{S5a}$$
$$b^{\mathrm{con}} = b^{\mathrm{sup}} \sum_{i=1}^{N} g(z_i). \tag{S5b}$$

When the temperature is not uniform along the z direction (i.e. temperature gradients are present), the relationship between the dye fluorescence intensity and the temperature can be expressed as

$$I_z^{\mathrm{con}} = a^{\mathrm{con}} T^{\mathrm{con}} + b^{\mathrm{con}} = \sum_{i=1}^{N} I_{z_i}^{\mathrm{sup}} g(z_i), \tag{S6}$$

where T^{con} is the experimentally measured temperature with convoluted intensity. After inserting Eq. (S3a), Eq. (S6) becomes

$$a^{\mathrm{con}} T^{\mathrm{con}} + b^{\mathrm{con}} = a^{\mathrm{sup}} \sum_{i=1}^{N} T(z_i) g(z_i) + b^{\mathrm{sup}} \sum_{i=1}^{N} g(z_i). \tag{S7}$$

Using the relationship between super-resolution and convoluted coefficients found in Eq. (S5), Eq. (S7) can be reduced to

$$T^{\mathrm{con}} = \frac{\sum_{i=1}^{N} T(z_i) g(z_i)}{\sum_{i=1}^{N} g(z_i)}. \tag{S8}$$

Then T^{con} can be compared with the simulated temperature values using the above relationship with $T(z_i)$ known in simulation.

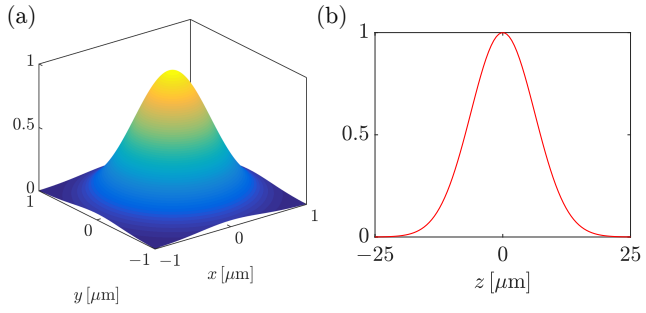

FIG. S5. The calculated point spread functions of the imaging system (a) in the x-y plane and (b) along the z-axis based on Gaussian approximations described by Eq. (S1).

S3. DETAILS OF THE NUMERICAL MODEL

The numerical model is the effective thermoviscous pressure acoustic model presented by Joergensen and Bruus [5] extended with heating from an external LED. The model is based on perturbation theory and simulates the unperturbed stationary temperature field T_0 in the solid and fluid, the acoustic time-varying pressure p_1 in the fluid and displacement $\boldsymbol{u}_1$ in the solid, and the second-order stationary streaming field $\boldsymbol{v}_2$ and pressure field p_2 in the fluid resulting from the non-linearity of the Navier-Stokes equation. The model of a glass-silicon-glass chip with a fluid channel of height $H = 370$ µm and width $W = 760$ µm is shown in Fig. S6. In the model we take advantage of the symmetries in the system and model a quarter of the channel, Fig. S6. In the y-z symmetry plane at $x = 0$ all fields are symmetric, and in the x-z symmetry plane at $y = 0$ the acoustic fields p_1 and $\boldsymbol{u}_1$ are anti-symmetric and the stationary fields T_0, $\boldsymbol{v}_2$, and p_2 are symmetric. The model parameters are listed in Table S2.

The actuation is modeled not as a full piezoelectric transducer as in Ref. [6], but merely as a boundary condition with a displacement $d_0 = 1$ nm and a frequency f_0 on the black actuation plane in Fig. S6 as in Ref. [7]. Note that using the symmetry planes, the model actually has anti-symmetric actuation regions, one on each side of the chip, which is not the case in the experimental setup. This does not change the shape of the pressure field in the fluid because we are at a fluid resonance completely dominated by a pressure component obeying the same anti-symmetry as the actuating regions.

During operation, a piezoelectric transducer generates heat, but this is neglected in the simulations for two reasons: (1) The necessary acoustic energy density is obtained in the system using a relatively low power consumption, and this assures that the heat generation is relatively small. (2) The heat from the transducer is lead through the top glass layer into the silicon layer, where it due to the high heat conductivity of silicon is uniformly distributed throughout the chip, leading to only a minute and nearly uniform temperature rise in the microchannel.

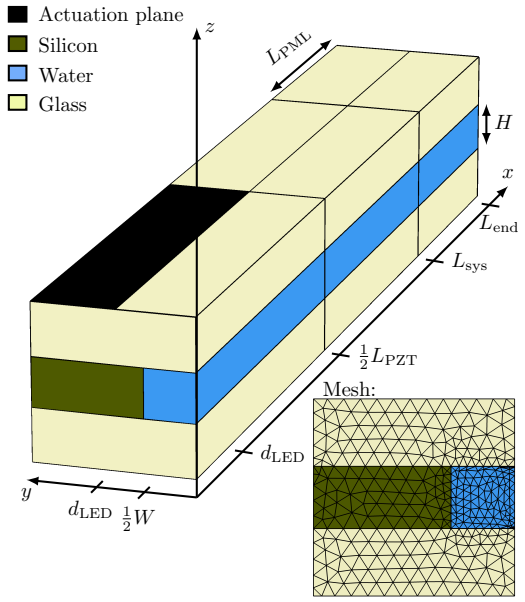

FIG. S6. Sketch of the numerical model of the acoustofluidic chip. Symmetry planes have been used so only a quarter of the channel is simulated. The model consists of a fluid domain with width W and height H, a solid domain (glass and silicon), and a special PML (perfectly matched layer) region where the travelling waves are artificially damped to mimic an infinitely long channel. The acoustic actuation is done on the actuation region (black) and the LED has its center at $x = 0$ and $y = 0$ and has half of the width d_{LED}. The mesh is shown in the y-z plane, which is swept along the x-axis so that the mesh node repeats itself with a distance of 51 µm.

TABLE S2. System parameters characterizing the geometry, the acoustic actuation, and the absorption of the LED spot.

Parameter	Symbol	Value	Unit
Geometry parameters:			
Fluid width	W	760	µm
Fluid height	H	370	µm
Actuation length	L_{PZT}	3.0	mm
System length	L_{sys}	5.5	mm
PML length	L_{PML}	1.75	mm
Total length	L_{end}	7.25	mm
Actuation paramters:			
Actuation amplitude	d_0	1.0	nm
Actuation frequency	f_0	0.957	MHz
LED paramters:			
Half width of the LED spot	d_{LED}	650	µm
Absorption coefficient	α	12.4	mm^{-1}

To avoid simulating the entire chip, the perfectly matched layer (PML) method is used to artificially damp travelling waves [8]. Thus, the model consists of an area of length L_{PZT} where a piezoelectric transducer actuates the chip at a frequency f_0 with an amplitude d_0, a part of length $L_{\mathrm{sys}} - L_{\mathrm{PZT}}$ where there are no actuation, and finally a section of length L_{PML} where the acoustic waves are artificially damped using a PML. For the PML to be valid, the distance $L_{\mathrm{sys}} - L_{\mathrm{PZT}}$ must be long enough for the travelling wave to develop so that the acoustic field does not depend on where the PML starts.

The real device has a long channel with a long piezoelectric transducer. To model the pressure field around the LED spot accurately, the length L_{PZT} must be larger than half of the LED spot width d_{LED}. The LED spot is modeled as a Gaussian beam with half of the beam width $d_{\mathrm{LED}} = 650$ µm (experimentally measured $d_{\mathrm{LED}} = 750 \pm 150$ µm using the knife-edge method [9]) and the absorption coefficient is set to $\alpha = 12.4\ \mathrm{mm}^{-1}$ to match the observed 99% absorption in the channel. The

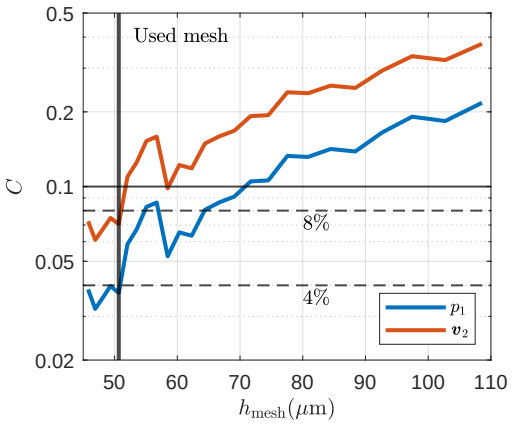

FIG. S7. A semi-logarithmic plot of the mesh convergence error C of Eq. (S10) versus mesh size h_{mesh} using a reference mesh simulated on a HPC-cluster with $h_{\mathrm{mesh}} = 38$ µm. The blue and red lines are C_{p_1} and C_{v_2} of the acosutic pressure and streaming, respectively. The thick black vertical line marks the mesh $h_{\mathrm{mesh}} = 51$ µm used for the simulations in the Letter, and the two dashed horizontal lines indicate the 4% and 8% levels.

Gaussian light intensity through the channel is given as,

$$I(x,y,z) = \frac{2P_{\mathrm{LED}}}{\pi d_{\mathrm{LED}}^2} \exp\left[-\frac{2(x^2+y^2)}{d_{\mathrm{LED}}^2} - \alpha\Big(z+\frac{1}{2}H\Big)\right], \tag{S9}$$

where P_{LED} is the total power of the LED and $-\frac{1}{2}H$ is the bottom of the channel where beam starts to be absorbed. In the solution, the heat absorption is given as $q(x,y,z) = \alpha I(x,y,z)$ for $-\frac{1}{2}H < z < \frac{1}{2}H$, while the absorption in the glass is neglected.

The entire model is implemented in COMSOL Multiphysics 5.6, with the governing equations and effective boundary conditions given by Joergensen and Bruus [5].

All calculations, except the mesh reference simulation, were performed on an HP-Z4 workstation with a processor Intel Core i9-7960X at 4.20 GHz and with 128 GB RAM. The model had 10^6 degrees of freedom in both the first- and second-order equations (acoustic and stationary fields). A mesh convergence analysis based on the standard L_2-norm error C_g [10],

$$C_g = \sqrt{\frac{\int |g(\boldsymbol{r}) - g_{\mathrm{ref}}(\boldsymbol{r})|^2 \,\mathrm{d}V}{\int |g_{\mathrm{ref}}(\boldsymbol{r})|^2 \,\mathrm{d}V}}, \tag{S10}$$

was performed for the pressure field $g = p_1$, and the streaming field $g = \boldsymbol{v}_2$, with a reference simulation g_{ref} computed on a HPC-cluster with a mesh size $h_{\mathrm{mesh}} = 38$ µm, see Fig. S7. The analysis shows that for a mesh with $h_{\mathrm{mesh}} = 51$ µm, shown in Fig. S6, the acoustic pressure field and the streaming field are converged to an L_2-error of 4% and 8%, respectively. The fairly good convergence obtained on the relatively coarse mesh shown in Fig. S6 is due to the use of the effective theory [5], because, (1) in the bulk, the body force driving the streaming contains no small length scales, and (2) as discussed in Refs. [11, 12], large canceling terms leading to numerical errors in the full model are explicitly removed when using the effective theory.

The numerical model uses cubic test functions for the streaming field and the acoustic pressure field, but quadratic test functions for the acoustic displacement field in the solid and the second-order pressure field.

S4. RAYLEIGH-BÉNARD CONVECTION

As a control experiment, the 3D Rayleigh-Bénard convection in the microchannel was investigated for a temperature gradient $G = 9.76$ K/mm across the channel measured at channel mid-height $z = 0$ (corresponding to $G = 13.78$ K/mm along the channel height obtained from simulation) when the sound field was off, and was compared with numerical simulation, see Fig. S8. Under the experimental conditions studied here, the Rayleigh-Bénard convection is in the laminar regime due to the low Rayleigh number $Ra = \frac{\rho g \beta}{\eta \alpha} H^3 \Delta T_0 = 5.06$, where ρ, β, η, and α are the density, thermal expansion coefficient, dynamic viscosity, and thermal diffusivity of water, respectively, and H is the channel height.

At the bottom center of the channel, the fluid expe-

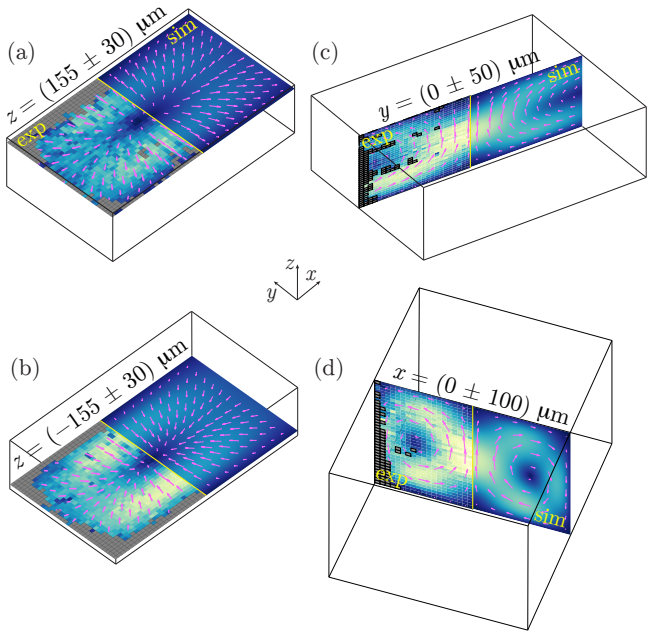

FIG. S8. (a)-(d) The measured (exp, left side) and simulated (sim, right side) pattern of Rayleigh-Bénard convection for $G = 9.76$ K/mm across the channel measured at $z = 0$ (corresponding to $G = 13.78$ K/mm along the channel height obtained from simulation), observed in different planes x-y horizontally, x-z vertically, and y-z vertically. The vector plot (magenta) in a given plane is the in-plane velocity and the color plot is its magnitude from 0 (dark blue) to 12.3 µm s^{-1} (yellow). Spatial bins with no experimental data points are excluded (gray).

riences the highest temperature due to light absorption, hence it expands and becomes less dense, resulting in a convection from the bottom to the top. The fluid is able to flow in both the x- and y-directions at the ceiling and circulate back along the bottom, creating two big rolls which can be viewed in the x-z and the y-z planes, see Fig. S8(c)-(d). The measured velocity amplitude of the Rayleigh-Bénard convection is $v_{\mathrm{con}} = (12.3 \pm 4.0)\ \mu\mathrm{m\,s}^{-1}$ ($9.9\ \mu\mathrm{m\,s}^{-1}$ in the simulation), which is almost two orders of magnitude lower than that of the thermoacoustic streaming.

[1] R. F. Kubin and A. N. Fletcher, Fluorescence quantum yields of some rhodamine dyes, J. Lumin. **27**, 455 (1982).

[2] D. A. Hinckley, P. G. Seybold, and D. P. Borris, Solvatochromism and thermochromism of rhodamine solutions, Spectrochim. Acta A Mol. Spectrosc. **42**, 747 (1986).

[3] J. Yoo, D. Mitchell, D. F. Davidson, and R. K. Hanson, Near-wall imaging using toluene-based planar laser-induced fluorescence in shock tube flow, Shock Waves **21**, 523 (2011).

[4] B. Zhang, J. Zerubia, and J.-C. Olivo-Marin, Gaussian approximations of fluorescence microscope point-spread function models, Appl. Opt. **46**, 1819 (2007).

[5] J. H. Joergensen and H. Bruus, Theory of pressure acoustics with thermoviscous boundary layers and streaming in elastic cavities, J. Acoust. Soc. Am. **149**, 3599 (2021).

[6] N. R. Skov, J. S. Bach, B. G. Winckelmann, and H. Bruus, 3D modeling of acoustofluidics in a liquid-filled cavity including streaming, viscous boundary layers, surrounding solids, and a piezoelectric transducer, AIMS Mathematics **4**, 99 (2019).

[7] M. W. H. Ley and H. Bruus, Three-dimensional numerical modeling of acoustic trapping in glass capillaries, Phys. Rev. Appl. **8**, 024020 (2017).

[8] A. Bermúdez, L. Hervella-Nieto, A. Prieto, and R. Rodríguez, An optimal perfectly matched layer with unbounded absorbing function for time-harmonic acoustic scattering problems, J. Comput. Phys. **223**, 469 (2007).

[9] J. Arnaud, W. Hubbard, G. Mandeville, B. De la Claviere, E. Franke, and J. Franke, Technique for fast measurement of gaussian laser beam parameters, Appl. Opt. **10**, 2775 (1971).

[10] P. B. Muller, R. Barnkob, M. J. H. Jensen, and H. Bruus, A numerical study of microparticle acoustophoresis driven by acoustic radiation forces and streaming-induced drag forces, Lab Chip **12**, 4617 (2012).

[11] A. Riaud, M. Baudoin, O. Bou Matar, J.-L. Thomas, and P. Brunet, On the influence of viscosity and caustics on acoustic streaming in sessile droplets: an experimental and a numerical study with a cost-effective method, J. Fluid Mech. **821**, 384 (2017).

[12] J. S. Bach and H. Bruus, Theory of pressure acoustics with viscous boundary layers and streaming in curved elastic cavities, J. Acoust. Soc. Am. **144**, 766 (2018).